Journal of
Materials Chemistry C

PAPER

View Article Online
View Journal

Check for updates

Cite this: DOI: 10.1039/d4tc05507a

Received 31st December 2024,
Accepted 17th June 2025

DOI: 10.1039/d4tc05507a

rsc.li/materials-c

Thermally driven morphology and lattice transformation of NiCo alloy for accelerating electrocatalytic water splitting†

Qingyi Qian,[a] Lixia Li,[a] Jiamin Liu,[a] Xi Duo,*[a] Ruifang Yang,[c] Xiaowei Li,[a] Quanquan Shi,[a] Xingkai Zhang[b] and Bo Hai*[a]

In the water-splitting process, the OER is a slow four-electron transfer process, and the overall efficiency of the water-splitting performance is low. A large reaction activation energy is thus required to overcome the high reaction energy barrier. To address this issue, we adjusted the external environment to provide thermal assistance, which increased the catalyst activity. Thermal assistance reduced the HER or OER overpotential of the Ni : Co = 1.5 : 1 catalyst during water electrolysis, achieving an HER overpotential of 48 mV and an OER overpotential of 296 mV at 10 mA cm^{-2} at 60 °C. The results reveal changes in both the morphology and crystal phase during the reaction. When the temperature was returned to 20 °C after heating, the activity of the catalyst was significantly higher than that before the temperature rise due to changes in the morphology and lattice.

Introduction

The carbon neutrality goal and issues such as global environmental pollution and the fossil energy crisis have become increasingly critical for sustainable life on earth.[1,2] To address these issues, new forms of energy are being researched and developed.[3] Hydrogen, which has a high specific-energy-density and is non-polluting, is being heavily researched.[4] Among the many methods of hydrogen production, electrolytic water hydrogen production has the advantages of simple operation and environmental compatibility, and has been studied extensively.[5–7] However, in real operating environments, the power required is typically 1.8 V, which is higher than the theoretical value of 1.23 V, resulting in a large amount of wasted energy.[8–10] Since the oxygen evolution reaction (OER) is a sluggish four-electron transfer process, the overall efficiency of water-splitting performance is reduced.[11,12] This is the main reason for the high working potential. OER has a high reaction energy barrier and a large reaction activation energy is required to enable efficient water splitting.[8,13]

Active electrocatalyst materials for the hydrogen evolution reaction (HER) and OER are in high demand;[14] however, the development of electrocatalysts that can combine HER catalytic activity with excellent OER activity is difficult. Although precious metal catalysts exhibit excellent water-splitting activity, their high price and low reserves severely limit their commercial use.[15–17] Inexpensive 3d transition metals exhibit excellent catalytic activity and have been investigated extensively.[18,19] Chavan *et al.* reported a nanoporous carbon (NNC)-based electrocatalytic system modified with spherical Ni/NiO nanoparticles, which demonstrated extremely high urea electrooxidation activity.[20] Narwade *et al.* prepared the face-centered cubic crystal structure Ni/NiO@rGO by chemical synthesis for electrochemical water splitting reactions, which showed a low Tafel slope over a wide range of pH values.[21] Tanwade *et al.* chemically synthesized highly dispersed nickel oxide nanoparticles (NiO NPs) on polyaniline (NiO-PanI) that exhibited excellent electrocatalytic activity, which was attributed to the availability of additional anchor localization sites, synergistic interactions between NiO and polyaniline, and improved overall electrical conductivity of the nanocomposite.[22] However, the performance of these materials is still not comparable to those of precious metal catalysts.[23]

To address this problem, 3d transition metal electronic structures have been modified through element doping. On the other hand, researchers are increasingly focusing not only on the intrinsic activity of the catalysts themselves, but also on

---

[a] *College of Science a & College of Material Science and Art Design, Inner Mongolia Agricultural University, Hohhot 010018, China. E-mail: duoxi@imau.edu.cn, haibo@imau.edu.can*

[b] *Key Laboratory of Science and Technology on Wear and Protection of Materials, Lanzhou Institute of Chemical Physics, Chinese Academy of Sciences, Lanzhou 730000, China*

[c] *Management Center of Laboratory and Equipment, Inner Mongolia Agricultural University, Hohhot 010018, China*

† Electronic supplementary information (ESI) available. See DOI: **https://doi.org/10.1039/d4tc05507a**

adjusting the external environment to enhance catalytic performance. For example, the use of electric and magnetic fields, strain and light have been studied.[24] Among the numerous field-assisted methods for increasing electrocatalytic activity, numerous reports on the effect of heat on catalytic performance have been published.

Electrocatalytic HER and OER are electrochemical processes that are dominated by kinetic energy barriers and mass transport.[25] Therefore, their reaction rates are highly sensitive to the operating temperature. This illustrates the importance of heat for modifying the catalytic activity. During the electrocatalytic reaction, thermal activation also enables mitigation of the overpotential resulting from kinetic barriers surpassing thermodynamic barriers. The incorporation of thermal chemistry concepts into electrocatalysis presents an opportunity for synergistic control over these complex multistep catalytic processes.[26] The reversible cell voltage of water electrolysers decreases with increasing temperature due to the positive entropy of the water-splitting reaction.[5]

Foroughi *et al.* studied the electrocatalytic HER and OER activities under both the absence (silent) and presence of ultrasound conditions, as well as at different electrolyte temperatures (T = 25, 40 and 60 °C). The results indicated that as the temperature increases, the influence of ultrasound on catalyst activity decreases. This result was ascribed to the efficient removal of gas bubbles from the electrode surface and the dispersion of gas bubbles into the electrolyte; this effect depends upon the behaviour of the hydrogen and oxygen gas bubbles in alkaline media and can improve catalyst activity.[27] Piontek *et al.* showed that HER activity of $Fe_{4.5}Ni_{4.5}S_8$ catalyst increased at increased temperature. They reasoned that increasing the temperature decreased the charge transfer resistance, promoted the removal of H_2 bubbles, and accelerated the formation of active hydrogen.[28] Meyer *et al.* studied metal carbide-coated wires at medium temperatures (200–400 °C) and found that the activity in the hydrogen evolution reaction (HER) followed the order $WC > Pt \approx Mo_2C > NbC > TaC$ at 260 °C.[29] Grdeń *et al.* adopted chemically etched Ni foams as well as polished and chemically etched polycrystalline Ni rods for comparative analysis and studied the Tafel slope and temperature relationship in the $277\ K \leq T \leq 308\ K$ range.[30] Pierozynski and Mikolajczyk prepared Pd-modified nickel foam and found a significant dependence on temperature for the HER kinetics, which was manifested through greatly reduced values for the charge transfer resistance parameter, as well as substantially modified Tafel polarization curves.[31] Wang *et al.* designed and studied a promising candidate for HER using highly uniform Ru nanoparticles over N-doped carbon that operated over a wide pH range and could be applied over a broad range of temperatures from 0 °C to 60 °C, greatly extending its applicability.[32] Chen *et al.* found that hydrogen production increased with increasing temperature in their studies on pure water hydrogen production *versus* water temperature using Sc–Sn alloys.[33] Bhoj *et al.* investigated the effect of reflux condensation temperatures (100, 120 and 140 °C) on the morphology and electrocatalytic activity of $NiCo_2O_4$ nanosheets. At 10 mA cm^{-2}, the overpotentials of HER and OER were only 79 mV and 310 mV, respectively.[34]

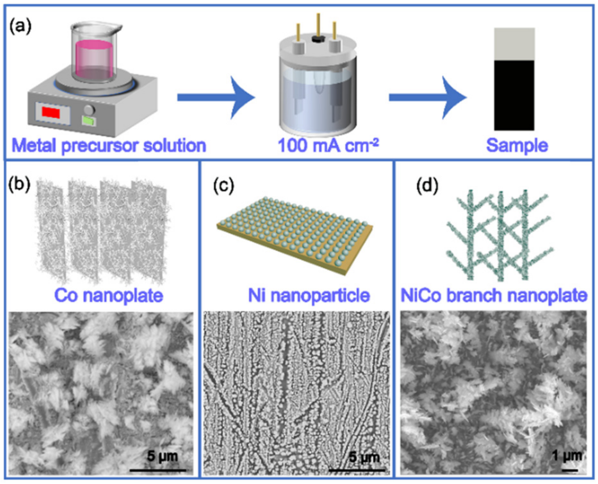

Fig. 1 (a) Catalyst preparation. (b)–(d) Schematic morphologies and SEM images of Co, Ni and Ni : Co = 1.5 : 1 catalyst samples, respectively.

The strategy of increasing the catalyst activity and decreasing the overpotential by increasing the temperature is thus feasible. We studied the HER and OER activities of NiCo catalysts with different ratios at different temperatures and explored the effects of composition and temperature on the activity of total hydrolysis of water to determine the underlying reasons for the change in catalytic activity. The metal nanocatalysts prepared are shown in Fig. 1a. In brief, thin films of Ni/Co alloys with different ratios were prepared by electrodeposition of a metal precursor solution at a current density of −100 mA cm^{-2}. The experimental results show that with an increase in temperature, the prepared catalyst exhibited an increase in water-splitting activity under alkaline conditions. The Ni : Co = 1.5 : 1 sample showed excellent HER and OER electrocatalytic activities with very low overpotential (47 and 296 mV, respectively) and a current density of 10 mA cm^{-2} at 1.0 M KOH. This study represents a proof-of-concept for multi-field coupling that could address pressing challenges that are difficult to solve using traditional electrocatalysis techniques. For the HER and OER catalysed reactions, it was demonstrated that the catalyst changed from the initial oxidation state to the hydroxide and hydroxyl oxide forms.

Results and discussion

The surface morphologies of the Co, metallic Ni, and NiCo alloy films were observed by scanning electron microscopy (SEM). Fig. 1b shows that the Co film is formed by stacking of Co nanosheets, with Co nanowires also distributed on the surface of the Co nanosheets. Fig. 1c shows a SEM image of Ni nanoparticles, which reveals that the Ni nanoparticles are uniformly distributed on the surface of the Cu sheet. The average size of each Ni nanoparticle is approximately 1 μm. Fig. 1d shows the surface morphology of the Ni : Co = 1.5 : 1

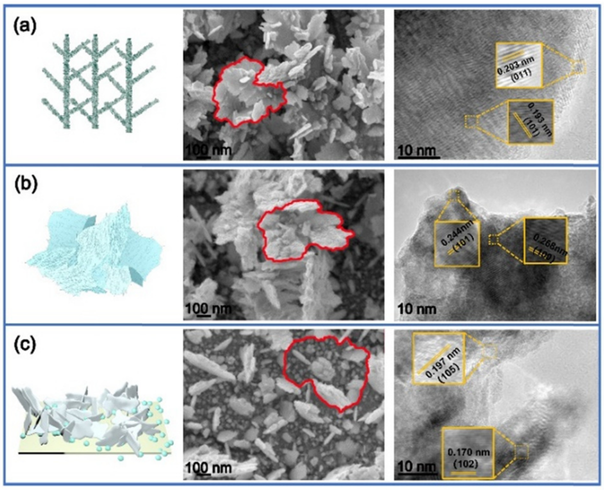

Fig. 2 (a) Schematic diagram of the morphology of the Ni : Co = 1.5 : 1 alloy and SEM and TEM imaging; (b) and (c) schematic diagrams of the morphologies of the NiCo alloy after HER and OER tests, as well as SEM and TEM imaging, respectively.

film, with NiCo nanosheets stacked in a branch structure. Ni, Co, and O elements are distributed uniformly over the Cu sheet surface, as shown in the EDS mapping images in Fig. S1 and S2 (ESI†). Ni, Co, and O atomic ratios were 46.5%, 31.33% and 22.17%, respectively. The Ni : Co ratio was approximately 1.58 : 1 as determined by ICP-OES analysis. The results are consistent with the NiCo metal salt mass and the EDS results listed in Table S1 (ESI†).

The surface morphology of the Ni : Co = 1.5 : 1 catalyst changed significantly when the catalysts were used in HER and OER reactions. After the HER reaction, the Ni : Co = 1.5 : 1 catalyst generated flocculated nanowires on the surface of the NiCo nanosheets as shown by SEM (Fig. 2b). After the OER reaction, SEM showed that the Ni Co nanosheets were loosened with a large number of nanoparticles generated (Fig. 2c). The HER and OER of the Ni : Co = 1.5 : 1 catalyst were tested three times with LSV at different temperatures (20 °C, 30 °C, 40 °C, 50 °C, 60 °C) as shown in Fig. S3 and S4(a)–(e) (ESI†). The morphology of the catalyst did not change significantly at different temperatures, but the particle size of the catalyst was reduced. This exposed more active sites on the catalyst, which increased the activity.

Further research through TEM showed that the Ni (101) and (011) facets were transformed into NiCo hydroxide (100) and (101) facets in the HER process (Fig. 2b). The Ni (101) and (100) facets transform into NiCo hydroxide (102) and (105) facets in the OER process (Fig. 2c). The catalyst facets thus underwent phase transfer during HER and OER in the water-splitting process. In catalytic stabilization tests, after approximately 8 hours of HER, crystalline facets of (104) and (105) of $Co(OH)_2$ were observed (Fig. S3f, ESI†). In the OER process, the presence of (102) crystalline facets of $Co(OH)_2$ and (140) crystalline facets of CoOOH were observed, demonstrating a transition from the alloy phase to the hydroxide phase during the catalytic reaction (Fig. S4f, ESI†).

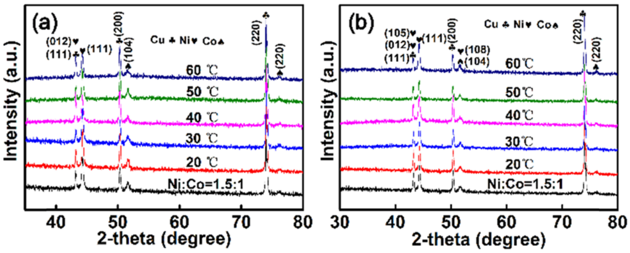

Fig. 3 (a) HER and (b) OER XRD images of the Ni : Co = 1.5 : 1 catalyst after three LSV tests at different temperatures.

The Ni : Co = 1.5 : 1 alloy films and samples were subjected to three LSV experiments at different temperatures (20 °C, 30 °C, 40 °C, 50 °C, 60 °C) and characterized by XRD; the results are shown in Fig. 3. It can be seen that the peak positions of the six groups of samples remain basically unchanged. The peak at 43.3° may be ascribed to Cu (111) and NiO (012), the peak at 44.3° stems from Ni (111), the peak at 50.4° is from Cu (200), the peak at 51.6° may be from $Co(OH)_2$ (104), the peak at 74.1° is from Cu (220), and the peak at 75.9° is from Co (220). During the OER process, the peaks at 43.3° and 51.6° may also be ascribed to (105) and (108) of NiOOH. The presence of crystalline surfaces of different elements at the same peak position may be due to overlapping peaks.

The elemental composition and valence states were analysed by X-ray photoelectron spectroscopy for the metal Ni, Co, and Ni : Co = 1.5 : 1 alloy films. The elements of Ni, Co, and O were detected in the survey spectra shown in Fig. S7, S8 and S9 (ESI†), respectively. The results indicate that Ni and Co elements were successfully deposited on the surface of the copper sheet.

Analysis of the elemental composition and valence state of the Co film (Fig. 4a) revealed Co $2p_{3/2}$ peaks for Co at 781.0 eV and 782.5 eV, which corresponded to Co^{3+} and Co^{2+}, respectively. The Co $2p_{1/2}$ peaks at 797.3 eV and 802.3 eV corresponded to the oxide peaks of Co. Two satellite peaks of Co were located at 786.6 eV and 804.6 eV. The Co $2p_{3/2}$ peaks in the NiCo alloys were at 777.8 eV and 781.1 eV, corresponding to metal Co^{3+} and Co^{2+}, and the Co satellite peak was located at 785.9 eV; the Co $2p_{1/2}$ peaks were located at 797.2 eV and 802

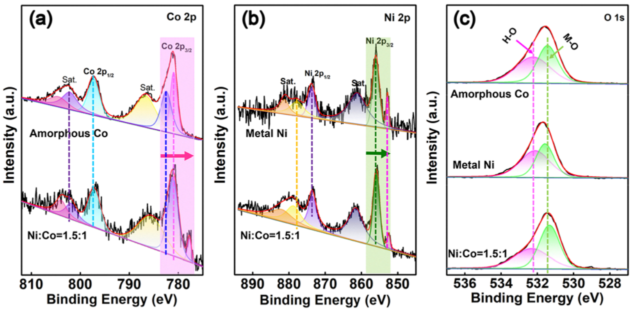

Fig. 4 (a) Shows the Co 2p peak of the Co and Ni : Co = 1.5 : 1 alloy, (b) shows the Ni 2p peak of the Ni and Ni : Co = 1.5 : 1 alloy, and (c) shows the O 1s peak of the Co, Ni and Ni : Co = 1.5 : 1 alloy.

eV, corresponding to Co^{3+}, Co^{2+}, and the Co satellite peak was located at 804 eV. Compared to Co, there was a significant negative shift of peaks for Co^{3+} and Co^{2+} in the $2p_{3/2}$ spectrum of elemental Co in the alloy. In the metal Ni film, the $2p_{3/2}$ Ni peaks were located at 852.8 eV, 856.1 eV, and 861.2 eV, corresponding to the metal Ni, the oxides of Ni (Ni^{2+}, Ni^{3+}) and the satellite peaks, respectively. Ni $2p_{1/2}$ peaks were located at 873.8 eV, 877.9 eV, and 881.3 eV also corresponding to the metal Ni, the oxides of Ni (Ni^{2+}, Ni^{3+}) and the satellite peak species of Ni. The Ni $2p_{3/2}$ peaks in the NiCo alloys were located at 852.5 eV, 855.9 eV, and 861.6 eV, which correspond to metal Ni, oxides of Ni (Ni^{2+}, Ni^{3+}) and satellite peaks of Ni, respectively. The Ni $2p_{1/2}$ peaks were located at 873.6 eV, 878.9 eV, and 882.5 eV, which corresponds to monomeric Ni, oxides of Ni (Ni^{2+}, Ni^{3+}), and satellite peaks of Ni, respectively. The valence state of the Ni element is shown in Fig. 4b.

Post-electrocatalytic characterization of the NiCo alloy films after HER and OER processes revealed significant electronic state modifications (see the ESI,† Fig. S10 and S11). XPS analysis demonstrated a positive binding energy shift of 2.0–2.3 eV for the Ni^{2+}/Ni^{3+} oxide species in the Ni $2p_{3/2}$ region (from initial 855.9 eV to 857.9 eV and 858.2 eV post-HER and OER, respectively), accompanied by a corresponding reduction in peak area from 20.00% to 19.4% and 4.3% (Table S2, ESI†). Concomitantly, the metallic Ni component exhibited binding energy shifts from 873.6 eV to 872.5 eV (HER) and 873.4 eV (OER), with its relative abundance decreasing from 16.6% to 8.4% and 16.1%, respectively.

These chemical state transformations can be mechanistically rationalized by considering alkaline electrolysis processes. During HER operation, metallic Ni undergoes electron acquisition and subsequently combines with hydroxyl radicals generated through Volmer and Heyrovsky reaction steps, leading to $Ni(OH)_2$ formation. Conversely, under OER conditions, Ni^{2+} species interact with reactive OH* intermediates, undergoing further oxidation to form NiOOH phases, which is a conclusion that is corroborated by complementary XRD analysis (Fig. 3b).

Parallel cobalt speciation analysis revealed notable electronic state alterations: The Co $2p_{1/2}$ metallic component maintained its binding energy at 797.2 eV post-HER while shifting to 796.7 eV after OER, with relative abundance increasing from 17.6% to 20.8% and 25.7%. Conversely, the Co^{2+} species exhibited a 3.7–4.0 eV positive binding energy shift (781.1 eV → 784.8 eV and 783.0 eV) accompanied by reduced peak area contributions from 32.6% to 18.6% and 21.5% following HER and OER processes, respectively (Table S2, ESI†). These coordinated changes in both nickel and cobalt electronic states demonstrate the dynamic surface reconstruction and valence state evolution during electrocatalytic operation.

The metal–oxygen bonds of O 1s in Co, metallic Ni and Ni : Co = 1.5 : 1 alloys are located at 531.4 eV, 531.6 eV and 531.3 eV,[35,36] respectively, and H–O bonds are located at 532.3 eV, 532.1 eV, and 532.3 eV (Fig. 4c),[37] respectively. There is a significant change between the XPS image of Co element in the two types of Co film and there is a slight shift in the Ni peaks for the two types of Ni film. For the three kinds of films, the O element peak shifts slightly, which demonstrates the existence of electron transfer interactions between the three metal elements Ni, Co and O.

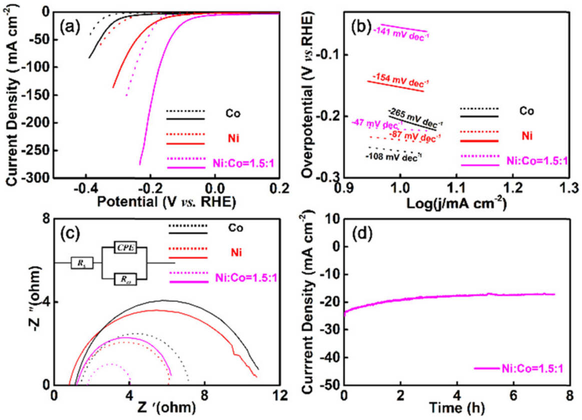

Fig. 5 HER performance of different samples in 1.0 M KOH. (a) LSV curves of samples of Co, metal Ni and Ni : Co = 1.5 : 1 alloy. (b) Tafel plot of samples of Co, metal Ni and Ni : Co = 1.5 : 1 alloy. (c) EIS spectra of Co, metal Ni and Ni : Co = 1.5 : 1. (d) The *i*–*t* test to determine Ni : Co = 1.5 : 1 alloy stability. The solid and dashed lines indicate 60 °C and 20 °C conditions, respectively.

The HER and OER catalyst activity was evaluated by electrochemical testing. Catalyst samples with different Ni and Co ratios were used as working electrodes, Ag/AgCl electrodes were used as reference electrodes, and carbon rods were used as counter electrodes. The electrochemical tests were conducted in 1 M KOH solutions. The LSV of HER scanning range was set from −1.5 V to −0.5 V (*vs.* Ag/AgCl), and the scanning rate was 5 mV s^{-1}; the results of the LSV tests are shown in Fig. 5a and Fig. S12 (dashed lines) (ESI†) (*iR* compensation = 90%). During the HER reaction process, the Ni : Co = 1.5 : 1 sample exhibited the best HER catalytic activity, with an overpotential of only 166 mV at 10 mA cm^{-2}. The overpotentials of Co film, metal Ni film and samples with Ni : Co ratios of 1 : 1 and 2 : 1 were 342 mV, 262 mV, 182 mV and 220 mV, respectively.

At 60 °C, the Ni : Co = 1.5 : 1 had the best HER catalyst activity of all samples, with an overpotential of only 47 mV at 10 mA cm^{-2}; the other four samples exhibited overpotentials of 197 mV, 149 mV, 64 mV, and 85 mV, respectively, at 10 mA cm^{-2}. The results are shown in Fig. 5a and Fig. S12 (solid lines) (ESI†). The HER activity process improved by increasing the temperature of the electrolyte. To investigate the relationship between temperature and HER catalytic performance, the HER activities at five temperature gradients were explored separately. As shown in Fig. S13 (ESI†), the HER activity of the Ni : Co = 1.5 : 1 sample improved as the sample temperature was increased to 20 °C, 30 °C, 40 °C, 50 °C and 60 °C; the Ni : Co = 1.5 : 1 sample overpotential was 221 mV, 161 mV, 120 mV, 96 mV, 47 mV, respectively. The results show that the temperature increase benefited HER catalyst activity. When the temperature returned to 20 °C, the LSV of the catalyst showed that the HER activity was increased compared to that in the initial 20 °C test (Fig. S14, ESI†).

A Tafel slope was constructed to describe HER catalyst activity dynamics. At 20 °C, the Tafel slope for Co, Ni and Ni : Co = 1.5 : 1 was −108 mV dec^{-1}, −87 mV dec^{-1} and

-47 mV dec^{-1}, respectively (Fig. 5b, dashed lines). The results showed that the Ni : Co = 1.5 : 1 sample had the best reaction dynamics and exhibited excellent conductivity. Notably, at elevated temperatures, the Tafel slope was significantly increased (Fig. 5b, solid lines). However, the Tafel slope still exhibited the same trends of Ni : Co = 1.5 : 1 (-141 mV dec^{-1}) < Ni (-154 mV dec^{-1}) < Co (-256 mV dec^{-1}). Fig. S15 (ESI†) presents Tafel plots at temperatures in the range of $293\ \text{K} \leq T \leq 343\ \text{K}$.

The results reveal a linear relationship for the Tafel slope over the entire set of temperatures (Fig. S16, ESI†). The slope of the Tafel plot is expressed by eqn (2), indicating that it should depend linearly on T:[30]

$$\eta = a + b \times \log j \tag{1}$$

$$b = (2.303 \times R \times T)/(\alpha \times F) \tag{2}$$

where α is the charge transfer coefficient, R is the gas constant, F is the Faraday constant, and j is the current density.

During the HER process, the reason for the increase in the Tafel slope as the temperature rises might be that at low temperatures, the rate determining step (RDS) is an electrochemical step (electron transfer), and the Tafel slope is relatively low, whereas at high temperatures, the RDS involves chemical steps (such as adsorption/desorption or surface reorganization), resulting in an increase in the slope.[38]

Three elementary reactions are typically involved in the HER in alkaline solutions (Scheme 1). The Volmer adsorption reaction is the first step, which forms adsorbed hydrogen (H*). The H* may then undergo either an electrochemical desorption step (Heyrovsky reaction) or a recombination step of H* (Tafel reaction) on the catalyst (Tafel slope of 30 mV dec^{-1}).

According to Tafel slope range, we infer that the HER process of this catalyst is likely to occur by a Volmer–Heyrovsky mechanism.

Electrochemical impedance spectroscopy (EIS) was used to probe the charge transfer resistance and electron transfer rate of the catalyst; the results are presented in Fig. 5c (solid and dashed lines). Under the same temperature conditions, the impedance radius exhibits the trend of Co > Ni > Ni : Co = 1.5 : 1. Ni : Co = 1.5 : 1 exhibited the highest conductivity. The EIS radii of Co, Ni, and Ni : Co = 1.5 : 1 increased significantly when the temperature was increased from 20 °C to 60 °C, as shown by the solid and dashed lines in Fig. 5c. Further exploration revealed that the EIS increased as the Ni : Co = 1.5 : 1 sample temperatures was increased to 20 °C, 30 °C, 40 °C, 50 °C and 60 °C (Fig. S17, ESI†). The EIS impedance radius gradually increased and the conductivity of the catalyst gradually decreased, probably due to the poor conductivity and high charge transfer resistance of the generated hydroxide.[36,37] At the same time, the solution resistance (R_s) between the reference and working electrodes decreased gradually with increasing temperature. Fig. S18–S22 (ESI†) compares the LSV curves of the Ni : Co = 1.5 : 1 sample before and after *iR* compensation at 20 °C, 30 °C, 40 °C, 50 °C and 60 °C, which show that the *iR* compensation potential decreases with increasing temperature, and η_s is gradually reduced.

$$H_2O + e^- \rightarrow H^* + OH^- \quad (1)\ \text{Volmer}$$

$$H_2O + e^- + H^* \rightarrow H_2 + OH^- \quad (2)\ \text{Heyrovsky}$$

$$H^* + H^* \rightarrow H_2 \quad (3)\ \text{Tafel (30 mV dec}^{-1}\text{)}$$

Scheme 1 Hydrogen evolution reaction mechanism in alkaline medium.

For a given electrode process at a certain potential E, the concentrations of reactant and product can be linked by the Nernst equation:[39,40]

$$E = E^{\theta'} + [(RT/(nF))]\cdot\ln(C_o/C_R)$$

where E is the electrode process at a certain potential, $E^{\theta'}$ is the formal potential of an overall reaction, R is the gas constant, F is the Faraday constant, n is the electron transfer number, and C_o/C_R is the concentration of oxidized/reduced species in the system. The working potential equation is expressed by eqn (2), which indicates that E should depend linearly on T and C_o/C_R. The catalyst reduces the reaction activation energy and thus the actual working potential. When C_o/C_R and working potential are a fixed value, temperature is inversely proportional to potential; the higher the temperature, the lower the actual operating potential.[41]

$$E = 1.23 + |\eta_a| + |\eta_c| + |\eta_s|$$

$$E_{(\text{cathode})} = |\eta_c| + |\eta_s|$$

where η_a and η_c indicate the inherent energy barrier potential of the anode and cathode, respectively, and η_s indicates the potential increase due to the influence of solution resistance, contact resistance and other system resistance. The η_a, η_c represents the overpotential generated by overcoming the inherent energy barrier of the material, which can be improved by modifying the electrode material.

$$\eta_s = R_s \times j$$

According to S2, R_s decreases with increasing temperature. The current density (j) is also a function of temperature and is inversely proportional to temperature, $\eta_s = R_s \times j$ decreases with increasing temperature.

The catalyst stability was studied by plotting the *i*–*t* slope. The Ni : Co = 1.5 : 1 sample exhibited good stability, with a small decrease in catalyst activity detected after 8 hours of constant potential at 20 mA cm^{-2}. The results show that the Ni : Co = 1.5 : 1 catalyst exhibited high catalytic stability (Fig. 5d).

The catalyst activity for the OER was evaluated by electrochemical testing. Catalyst samples with different Ni and Co ratios were used as working electrodes. The electrochemical tests were conducted in 1 M KOH solutions. The scanning range of LSV was set from 0 V to 1 V (*vs.* Ag/AgCl), and the scanning rate was 5 mV s^{-1}. The results of the LSV tests are shown in Fig. 6(a) (*iR* compensation = 90%). During the OER reaction, the Co film exhibited the best OER catalytic activity; at 10 mA cm^{-2}, the overpotential was 365 mV. The metal Ni film had the worst OER activity, with an overpotential of 482 mV,

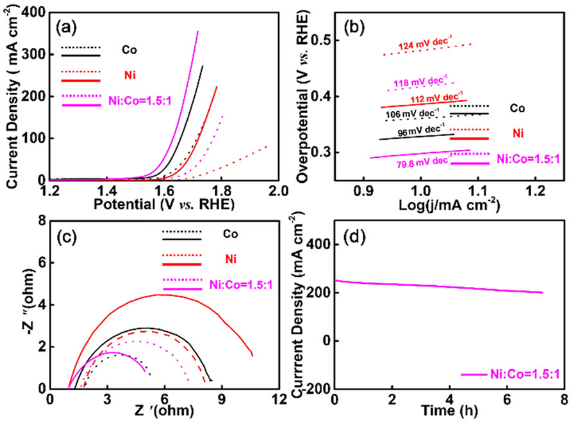

Fig. 6 OER performance of different samples in 1.0 m KOH. (a) LSV curves of samples of Co, metal Ni and Ni : Co = 1.5 : 1 alloy. (b) Tafel plot of samples of Co, metal Ni and Ni : Co = 1.5 : 1 alloy. (c) EIS spectra of Co, metal Ni and Ni : Co = 1.5 : 1; (d) *i–t* test to determine Ni : Co = 1.5 : 1 alloy stability. The solid and dashed lines represent 60 °C and 20 °C conditions, respectively.

and the overpotentials of samples with Ni/Co ratios of 1 : 1, 1.5 : 1, and 2 : 1 were 398 mV, 418 mV, and 426 mV, respectively. The OER results are shown as dashed lines in Fig. 6a and Fig. S23 (ESI†). At elevated temperatures of up to 60 °C, the OER activity changed for all the Ni/Co samples. The OER catalytic activity increased significantly compared with that at 20 °C. The best OER catalytic activity was found for the sample with a Ni : Co ratio of 1.5 : 1, giving an overpotential of only 296 mV at 10 mA cm^{-2}; the overpotentials for the other four samples were 330 mV, 388 mV, 320 mV, and 316 mV, respectively. The results are plotted as solid lines in Fig. 5a and Fig. S23 (ESI†).

In order to study the relationship between OER catalyst activity and temperature, the 1.5 : 1 catalyst activity was studied at five temperature gradients of 20 °C, 30 °C, 40 °C, 50 °C, 60 °C, which gave overpotentials of 419 mV, 354 mV, 337 mV, 324 mV, 296 mV, respectively, at 10 mA cm^{-2}. Thus, the catalyst activity increased with increasing temperature. The results are shown in Fig. S24 (ESI†). When the electrolyte temperature returned to 20 °C, the LSV curve of the sample of Ni : Co = 1.5 : 1 (displayed as a red line in Fig. S25, ESI†) showed that the OER activity was significantly improved compared with the performance of the original Ni : Co = 1.5 : 1 catalyst, indicating that changes had occurred in the morphology and phase of the sample.

The Tafel slope was plotted to describe OER catalyst activity dynamics. At 20 °C, the Tafel slopes for the Co, Ni and Ni : Co = 1.5 : 1 samples were 106 mV dec^{-1}, 124 mV dec^{-1} and 118 mV dec^{-1}, respectively (dashed line in Fig. 6b). The Co sample had the best reaction dynamics. The EIS radii were Ni > Ni : Co = 1.5 : 1 > Co, illustrating that Co showed the fastest electron transfer rate (dashed line in Fig. 6c). At elevated temperature, the Tafel slope changes significantly. The EIS radius for Co, Ni and Ni : Co = 1.5 : 1 samples also changed significantly and the EIS radius of Ni, Co and Ni : Co = 1.5 : 1 showed a decreasing trend (Fig. 6c, solid line). The different temperature (20 °C, 30 °C, 40 °C, 50 °C and 60 °C) of Ni : Co = 1.5 : 1 sample was Tafel slope and EIS increase with temperature decrease by Fig. S26 and S27 (ESI†). However, at a certain temperature, no further change in the Tafel slope or EIS radius was observed. The catalyst stability was studied by plotting the *i–t* slope. The Ni : Co = 1.5 : 1 sample exhibited good stability, with a small decrease in catalyst activity detected after 8 hours of constant potential at 250 mA cm^{-2}. The Ni : Co = 1.5 : 1 catalyst demonstrated good catalytic stability with current density remaining above 200 mA cm^{-2} (Fig. 6d).

To further explore the relationship between temperature and catalytic activity, the electrochemically active area and intrinsic activity were calculated. We calculated the electrochemical surface area (ECSA) of catalysts with different Ni Co ratios from the electrochemical double layer capacitance (C_{dl}) of the electrodes, which is proportional to the slope of the capacitance current as a function of the scan rate, using cyclic voltammetry. For conductive compounds, ECSA is considered to be a reliable method for determining the active surface area of different conductive catalysts.[42]

At 20 °C, the NiCo alloy had the biggest ECSA of the three samples, metal Ni film ECSA had the least (*cf.* black line of Fig. S28, S30 and S32, ESI†). When the temperature reached 60 °C, the ECSA of the Co film, metallic Ni film and NiCo alloy film increased significantly, as shown by the red lines in Fig. S28, S30 and S32 (ESI†). After normalizing by unit area, the intrinsic activity of the Co active sites in the Co film showed a noticeable improvement (Fig. S29, ESI†). This enhancement in catalytic performance is attributed to both the increased electrochemical active area and the phase transfer from Co to CoOOH, which significantly boosted the intrinsic catalytic activity of the active sites. The catalytic performance of the Ni and NiCo alloy films were also enhanced, which may be due to the phase transfer generating intrinsic catalytically active sites and significantly enhanced ECSA (Fig. S31 and S33, ESI†).

The reason for the crystal phase transfer may be the reaction of metal oxide with OH^- during the electrocatalytic reaction to form a new compound. Switzer and co-workers reported that Co^{2+} and OH^- could form $Co(OH)_2$, which was electrodeposited onto the cathode.[43] Wang *et al.* converted vertically oriented Co-based nanorods *in situ* into $Co(OH)_2$@CoSe NRs by the combination of derived OH^- with Co^{2+} ions on the cathodic co-based nanorod precursors.[44] We inferred that the Co and Ni base-metal oxide may be transformed into $Co(OH)_2$ and $Ni(OH)_2$ during the *in situ* electrochemical and temperature change process. This may be an important reason for the change in catalyst morphology. The chemical reactions during the transformation to produce $Co(OH)_2$ and $Ni(OH)_2$ are shown in equations:

$$Co^{2+} + OH^- \rightarrow Co(OH)_2$$

$$Ni^{2+} + OH^- \rightarrow Ni(OH)_2$$

According to the literature, during the OER reaction, the stable crystalline phase of cobalt oxides is CoOOH (or Co_3O_4) at $E = +1.6$ V *vs.* RHE and pH 14.[45] In addition, operational XPS measurements showed that $Co(OH)_2$ was completely converted

$$* + OH^- \rightarrow OH^* + e^-$$
$$OH^* + OH^- \rightarrow O^* + H_2O + e^-$$
$$O^* + OH^- \rightarrow OOH^* + e^-$$
$$OOH^* + OH^- \rightarrow O_2 + H_2O + e^- + *$$

Scheme 2 Oxygen evolution reaction mechanism in alkaline medium.

into CoOOH in such an anodic potential region. $Co(OH)_2$ was converted into CoOOH lamellae, which facilitated the OER catalytic reaction process and improved the OER reactivity.[46] This helps to further explain the change in catalyst performance before and after warming the electrolyte: the catalyst phase transformed from the oxidized state to OOH. The chemical reactions during the transformation to produce $Co(OH)_2$ and $Ni(OH)_2$ are shown in equations:

$$Co(OH)_2 + OH^- \rightarrow CoOOH + H_2O + e^-$$

$$Ni(OH)_2 + OH^- \rightarrow NiOOH + H_2O + e^-$$

The overpotential was determined by assuming the OER mechanism with the following elementary steps (Scheme 2):

During the electrocatalytic reaction, as the temperature increases, the facets of the catalyst changes from the metal oxide to the hydroxide phase, and the ΔE ($\Delta G = \Delta E + \Delta E_{ZPE} - T\Delta S$) of the overall catalytic system changes (Fig. 7). $\eta_1 = \eta_2 + \eta_3$, η_2 is the potential difference between NiCo catalysts at the same temperature and the same current density due to changes in catalyst morphology and crystalline phase. η_3 is the potential change of catalyst with the same morphology and crystalline phase due to the difference of temperature. After the HER reaction, flocculated nanowires were generated on the surface of the catalyst nanosheets. After the OER reaction, the surface of the nanosheets became looser with the generation of many nanoparticles.

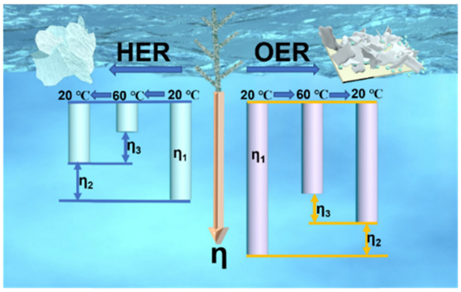

Fig. 7 Schematic of the change of the reaction process η.

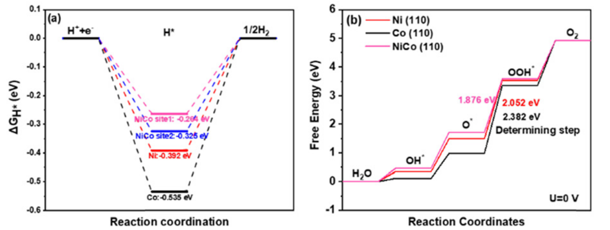

Fig. 8 (a) Calculated Gibbs free energy (ΔG_{H^*}) of the HER process on Ni (110), Co (110) and NiCo (110) surfaces. (b) Calculated free energy diagram for the OER on Ni (110), Co (110) and NiCo (110) surfaces at U = 0 V.

The electrochemical activity of NiCo catalysts was systematically investigated through density functional theory (DFT) calculations. Structural analysis revealed that both metallic Ni and Co adopt face-centered cubic (FCC) configurations with *Fm*3*m* space group symmetry in their elemental forms (see the Fig. S34a and b, ESI†). Intriguingly, theoretical simulations demonstrated that the binary Ni–Co system formed through precursor composite engineering crystallizes in a distinct cubic phase (*Fd*3*m* space group), as evidenced by the optimized Ni_3Co_2 structure shown in Fig. S34c (ESI†).

HER catalytic performance was quantitatively evaluated through hydrogen adsorption Gibbs free energy analysis ($|\Delta G_{H^*}|$) as presented in Fig. 8a and Table S3 (ESI†). Consistent with established theoretical frameworks,[47,48] optimal HER activity is achieved when $|\Delta G_{H^*}|$ approaches thermodynamic neutrality. DFT calculations revealed significant electronic structure modulation in the Ni : Co = 1.5 : 1 system (for structural details, see the Fig. S35, ESI†). Post-optimization analysis showed that the NiCo (110) facet exhibits a ΔG_{H^*} value of −0.264 eV, demonstrating substantial improvement compared to pure Ni (110) (−0.392 eV) and Co (110) (−0.535 eV) facets. This computational finding aligns with previous theoretical studies by Mohsenzadeh *et al.*,[49] confirming the NiCo (110) interface as the predominant active site.

Notably, the negative ΔG_{H^*} values suggest thermodynamically favorable hydrogen adsorption but kinetically hindered desorption processes, establishing hydrogen desorption as the rate-determining step. Comparative analysis revealed that the NiCo (110) facet possesses the smallest $|\Delta G_{H^*}|$ magnitude (0.264 eV), representing a 32.6% reduction compared to pure Ni (110). This cobalt-induced electronic modulation effectively shifts the rate-limiting step from adsorption to desorption while substantially lowering the activation energy barrier. The computational predictions exhibit remarkable consistency with experimentally observed enhancements in HER activity, validating the theoretical model.

The OER activity modulation mechanism of the NiCo system was elucidated through four-electron pathway Gibbs free energy analysis, as depicted in Fig. 8b, the Fig. S36 and Tables S4–S6 (ESI†). Computational results identified Ni sites as predominant active centers due to their lower activation barrier (2.052 eV) compared to Co sites (2.382 eV). Remarkably, the NiCo co-precipitated configuration ($Ni_{1.5}Co_1$) exhibited a further reduced energy barrier of 1.876 eV at the NiCo site 1, demonstrating superior catalytic activity over monometallic Ni and Co counterparts.

The overpotential (η) for each active site was derived by subtracting the thermodynamic equilibrium potential (1.23 V) from the total Gibbs free energy (Fig. 8b). Energy profiles at applied potentials U = 0 V and 1.23 V are demarcated by red, black, and pink lines for Ni, Co, and NiCo systems, respectively. Reaction pathway analysis revealed that the rate-determining step (RDS) universally corresponds to the $O^* \rightarrow OOH^*$ transformation (third reaction step). Specifically, the Ni (110) facet exhibited an activation barrier of 2.052 eV (η = 0.822 eV), while cobalt incorporation in the NiCo system significantly lowered the barrier to 1.876 eV (η = 0.646 eV), achieving a 21.4% reduction in overpotential.

This theoretical prediction of reduced activation energy aligns quantitatively with experimentally observed OER activity enhancement, establishing strong consistency between DFT simulations and empirical measurements. The synergistic electronic effects induced by Co doping effectively optimize intermediate adsorption energetics, thereby accelerating the kinetically sluggish OER process.

Conclusions

This comprehensive investigation systematically elucidates the structure–activity relationship and electrocatalytic mechanism of NiCo alloy catalysts with optimized Ni : Co ratios for efficient water splitting. The Ni : Co = 1.5 : 1 catalyst demonstrates exceptional bifunctional performance, achieving ultralow overpotentials of 48 mV (HER) and 296 mV (OER) at 10 mA cm^{-2} at elevated temperature (60 °C). Temperature-dependent studies reveal a dual role of thermal energy: while enhancing HER activity through accelerated charge transfer and reduced solution resistance, it simultaneously induces phase transitions from metallic alloys to hydroxides ($Ni(OH)_2/Co(OH)_2 \rightarrow$ NiOOH/CoOOH), which critically governs OER performance.

XPS and XRD analyses confirm dynamic surface reconstruction during electrocatalysis, where metallic Ni and Co undergo hydroxylation to form active hydroxide/oxyhydroxide species. Theoretical calculations provide atomic-level insights, identifying the NiCo (110) facet as the predominant active site with optimized hydrogen adsorption energy ($\Delta G_{H^*} = -0.264$ eV) and reduced OER activation barriers (1.876 eV *vs.* 2.052 eV for pure Ni). The cobalt-induced electronic modulation facilitates charge redistribution, shifting rate-limiting steps from hydrogen desorption (HER) to $O^* \rightarrow OOH^*$ transition (OER), thereby synchronously enhancing both half-reactions.

Notably, the catalyst exhibits remarkable stability, attributed to its adaptive surface morphology HER generates flocculated nanowires, while OER forms loosened nanostructures with abundant nanoparticles, with both configurations favoring active site exposure. This work establishes a rational design paradigm for transition metal alloy catalysts, emphasizing the synergistic interplay between composition optimization, temperature-mediated phase engineering, and electronic structure modulation for advanced energy conversion technologies.

Conflicts of interest

The authors declare that they have no competing financial interest.

Data availability

The authors confirm that the data supporting this article have been included as part of the manuscript.

Acknowledgements

We thank the Natural Science Foundation of Inner Mongolia Autonomous Region (2022MS02002) and the Natural Science Foundation of Inner Mongolia Autonomous Region of China (2023LHMS02007) for financial support.

Notes and references

1 Q. Zhao, Q. Qian, B. Zhang and X. Zhang, *Mater. Chem. Phys.*, 2021, **263**, 124412–124417.

2 D. Wang, Y. Xie and Z. Wu, *Nanotechnology*, 2019, **30**, 205401–205408.

3 T. Liu, Y. Liang, Q. Liu, X. Sun, Y. He and A. M. Asiri, *Electrochem. Commun.*, 2015, **60**, 92–96.

4 D. Wu, Y. Wei, X. Ren, X. Ji, Y. Liu, X. Guo, Z. Liu, A. M. Asiri, Q. Wei and X. Sun, *Adv. Mater.*, 2018, **30**, 1705366–1705372.

5 A. Ursua, L. M. Gandia and P. Sanchis, *Proc. IEEE*, 2012, **100**, 410–426.

6 R. Kothari, D. Buddhi and R. L. Sawhney, *Renewable Sustainable Energy Rev.*, 2008, **12**, 553–563.

7 Y. Lang, R. R. Arnepalli and A. Tiwari, *J. Nanosci. Nanotechnol.*, 2011, **11**, 3719–3739.

8 S. Du, Z. Ren, J. Zhang, J. Wu, W. Xi, J. Zhu and H. Fu, *Chem. Commun.*, 2015, **51**, 8066–8069.

9 A. Kubacka, M. Fernández-García and G. Colón, *Chem. Rev.*, 2011, **112**, 1555–1614.

10 M. Li, X. Wang, K. Liu, Z. Zhu, H. Guo, M. Li, H. Du, D. Sun, H. Li, K. Huang, Y. Tang and G. Fu, *Adv. Energy Mater.*, 2023, **13**, 2301162–2301174.

11 M. M. Najafpour, T. Ehrenberg, M. Wiechen and P. Kurz, *Angew. Chem., Int. Ed.*, 2010, **49**, 2233–2237.

12 V. B. R. Boppana and F. Jiao, *Chem. Commun.*, 2011, **47**, 8973–8975.

13 J. Wang, L. Han, B. Huang, Q. Shao, H. L. Xin and X. Huang, *Nat. Commun.*, 2019, **10**, 5692–5701.

14 V. Jose, E. Edison, W. W. Manalastas, S. Sreejith, J. M. Vianney Nsanzimana, M. Srinivasan and J.-M. Lee, *ACS Appl. Mater. Interfaces*, 2019, **11**, 39798–39808.

15 W. Sheng, H. A. Gasteiger and Y. Shao-Horn, *J. Electrochem. Soc.*, 2010, **157**, B1529–B1536.

16 P. Jiang, Q. Liu, Y. Liang, J. Tian, A. M. Asiri and X. Sun, *Angew. Chem.*, 2014, **126**, 13069–13073.

17 A. Shafaei Douk, H. Saravani and M. Noroozifar, *J. Alloys Compd.*, 2018, **739**, 882–891.

18 Y. Xu, R. Wang, Y. Zheng, L. Zhang, T. Jiao, Q. Peng and Z. Liu, *Appl. Surf. Sci.*, 2020, **509**, 145383–145392.

19 X. Lv, X. Li, C. Yang, X. Ding, Y. Zhang, Y. Z. Zheng, S. Li, X. Sun and X. Tao, *Adv. Funct. Mater.*, 2020, **30**, 1910830–1910839.

20 P. P. Chavan, P. D. Tanwade, V. S. Sapner and B. R. Sathe, *RSC Adv.*, 2023, **13**, 26940–26947.

21 S. S. Narwade, S. M. Mali, R. V. Digraskar, V. S. Sapner and B. R. Sathe, *Int. J. Hydrogen Energy*, 2019, **44**, 27001–27009.

22 P. D. Tanwade, A. V. Munde, B. B. Mulik, A. Adhikari, R. Patel and B. R. Sathe, *Energy Fuels*, 2023, **37**, 19959–19970.

23 T. Sun, J. Wang, C. Qiu, X. Ling, B. Tian, W. Chen and C. Su, *Adv. Sci.*, 2018, **5**, 1800036–1800044.

24 J. Yao, W. Huang, W. Fang, M. Kuang, N. Jia, H. Ren, D. Liu, C. Lv, C. Liu, J. Xu and Q. Yan, *Small Methods*, 2020, **4**, 2000494–2000517.

25 Y. Guo, T. Park, J. W. Yi, J. Henzie, J. Kim, Z. Wang, B. Jiang, Y. Bando, Y. Sugahara, J. Tang and Y. Yamauchi, *Adv. Mater.*, 2019, **31**, 1807134–18071067.

26 K. Liu, H. Li, M. Xie, P. Wang, Z. Jin, Y. Liu, M. Zhou, P. Li and G. Yu, *J. Am. Chem. Soc.*, 2024, **146**, 7779–7790.

27 F. Foroughi, C. Immanuel Bernäcker, L. Röntzsch and B. G. Pollet, *Ultrason. Sonochem.*, 2022, **84**, 105979–105992.

28 S. Piontek, C. Andronescu, A. Zaichenko, B. Konkena, K. Junge Puring, B. Marler, H. Antoni, I. Sinev, M. Muhler, D. Mollenhauer, B. Roldan Cuenya, W. Schuhmann and U.-P. Apfel, *ACS Catal.*, 2018, **8**, 987–996.

29 S. Meyer, A. V. Nikiforov, I. M. Petrushina, K. Köhler, E. Christensen, J. O. Jensen and N. J. Bjerrum, *Int. J. Hydrogen Energy*, 2015, **40**, 2905–2911.

30 M. Grdeń and G. Jerkiewicz, *Electrocatalysis*, 2019, **10**, 173–183.

31 B. Pierozynski and T. Mikolajczyk, *Electrocatalysis*, 2014, **6**, 51–59.

32 J. Wang, Z. Wei, S. Mao, H. Li and Y. Wang, *Energy Environ. Sci.*, 2018, **11**, 800–806.

33 H. Chen, X. Zhang, Y. Liu, C. Liu, L. Jin, H. Li, X. Dai and G. Liu, *Int. J. Hydrogen Energy*, 2024, **66**, 645–651.

34 P. K. Bhoj, G. P. Kamble, J. B. Yadav, T. D. Dongale, B. R. Sathe and A. V. Ghule, *Appl. Surf. Sci.*, 2024, **648**, 159083–159094.

35 X. Han, Q. Chen, H. Zhang, Y. Ni and L. Zhang, *Chem. Eng. J.*, 2019, **368**, 513–524.

36 M. Xie, K. Jia, J. Lu and R. Zhao, *CrystEngComm*, 2020, **22**, 546–553.

37 Q. Qian, G. Yu, Q. Zhao and X. Zhang, *New J. Chem.*, 2023, **47**, 1040–1044.

38 J. K. Nørskov, T. Bligaard, A. Logadottir, J. R. Kitchin, J. G. Chen, S. Pandelov and U. Stimming, *J. Electrochem. Soc.*, 2005, **152**, J23–J26.

39 Y. Jiao, Y. Zheng, M. Jaroniec and S. Z. Qiao, *Chem. Soc. Rev.*, 2015, **44**, 2060–2086.

40 A. J. Bard and L. R. Faulkner, *Electrochemical methods: fundamentals and applications*, John Wiley & Sons, Inc., New York, 2001, vol. 60.

41 H. Zhang, A. W. Maijenburg, X. Li, S. L. Schweizer and R. B. Wehrspohn, *Adv. Funct. Mater.*, 2020, **30**, 2003261–2003290.

42 S. Jung, C. C. L. McCrory, I. M. Ferrer, J. C. Peters and T. F. Jaramillo, *J. Mater. Chem. A*, 2016, **4**, 3068–3076.

43 Y.-C. Liu, J. A. Koza and J. A. Switzer, *Electrochim. Acta*, 2014, **140**, 359–365.

44 Y. Wang, Y. Yang, X. Wang, P. Li, H. Shao, T. Li, H. Liu, Q. Zheng, J. Hu, L. Duan, C. Hu and J. Liu, *Nanoscale Adv.*, 2020, **2**, 792–797.

45 M. Bajdich, M. García-Mota, A. Vojvodic, J. K. Nørskov and A. T. Bell, *J. Am. Chem. Soc.*, 2013, **135**, 13521–13530.

46 M. Favaro, J. Yang, S. Nappini, E. Magnano, F. M. Toma, E. J. Crumlin, J. Yano and I. D. Sharp, *J. Am. Chem. Soc.*, 2017, **139**, 8960–8970.

47 J. Su, Y. Yang, G. Xia, J. Chen, P. Jiang and Q. Chen, *Nat. Commun.*, 2017, **8**, 14969–14978.

48 P. Chen, K. Xu, S. Tao, T. Zhou, Y. Tong, H. Ding, L. Zhang, W. Chu, C. Wu and Y. Xie, *Adv. Mater.*, 2016, **28**, 7527–7532.

49 A. Mohsenzadeh, K. Bolton and T. Richards, *Surf. Sci.*, 2014, **627**, 1–10.